Geochemical Perspectives Letters

Termination of Cryogenian ironstone deposition by deep ocean euxinia

C. Wu, T. Yang, G.A. Shields, X. Bian, B. Gao, H. Ye, W. Li

Supplementary Information

The Supplementary Information includes:

- 1. Geological Background of the Xinyu Iron Formation
- 2. Petrography and Mineral Chemistry of the Xinyu Iron Formation
- 3. Analytical Methods and Data Tables
- Figures S-1 to S-10
- Tables S-1 to S-3
- Supplementary Information References

1. Geological Setting, Regional Geology and Stratigraphy

The South China Block consists of the Yangtze Block and the Cathaysia Block (Zhao and Cawood, 2012). These two blocks collided between the Late Mesoproterozoic to the earliest Neoproterozoic (Wang and Li, 2003; Wang *et al.*, 2014), leading to the formation of the ~1500km Jiangnan orogen (Wang *et al.*, 2014). Meso-Neoproterozoic sedimentary sequences widely developed around the Yangtze Block and along the northwestern Cathaysia Block, and consist of two main parts that are separated by a regional unconformity (Fig. S-1; Wang and Li., 2003; Wang *et al.*, 2012).

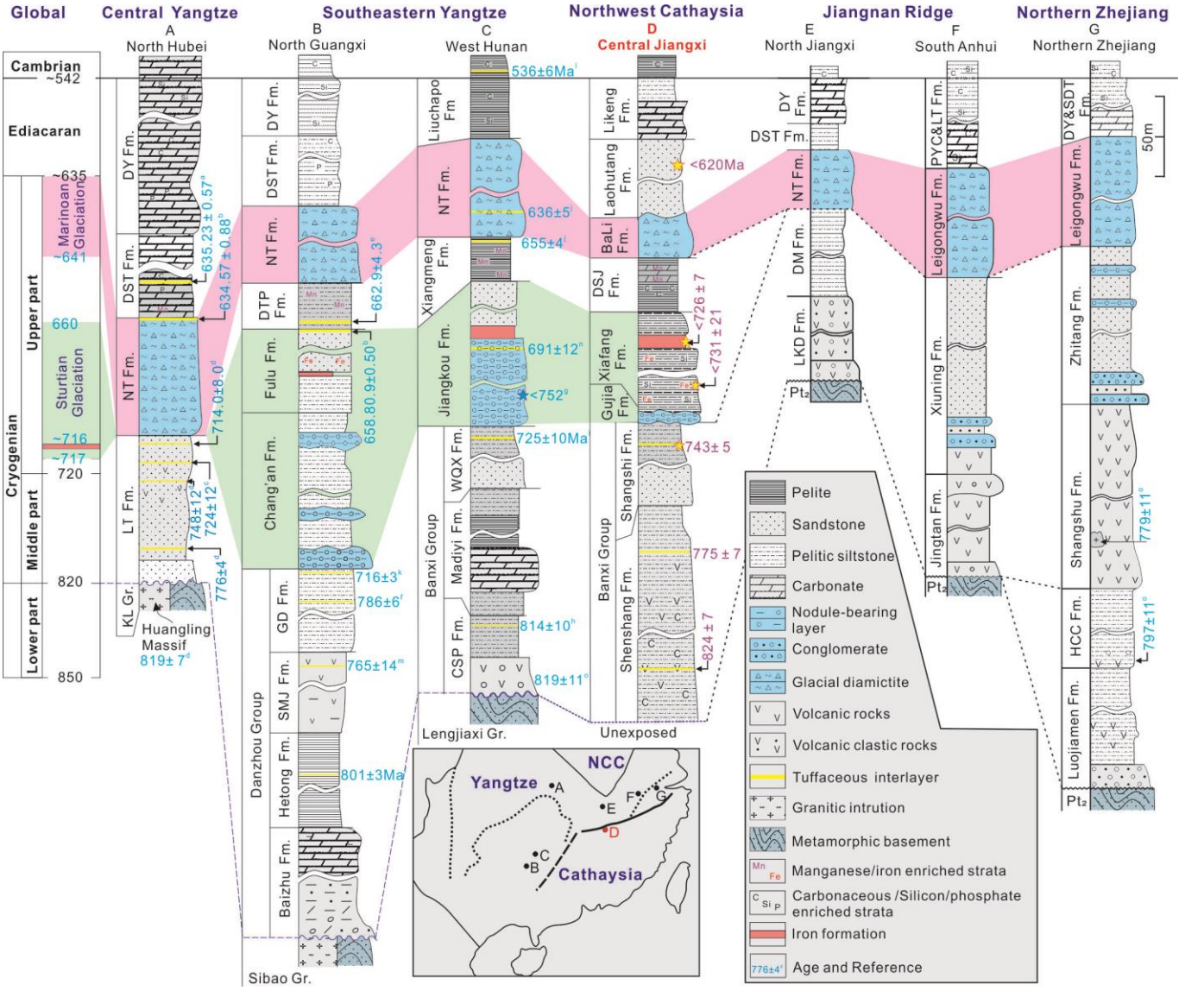

Figure S-1 Correlation of representative Neoproterozoic strata in South China (modified from Wang and Li, 2003; Yang *et al.*, 2012). NCC-North China Craton; WQX Fm.-Wuqiangxi formation; SMJ Fm.-Sanmengjie formation; CSP Fm.-Cangshuipu formation; GD Fm.-Gongdong formation; XM Fm.-Xiangmeng formation; DTP Fm.- Datangpo formation. KL Gr.-Kongling Group; NT Fm.-Nantuo formation; DST Fm.-Doushantuo formation; DY Fm.-Denying formation; LKD Fm.-Luokedong formation; DM Fm.-Dongmen formation; LGW Fm.-Leigongwu formation; PYC&LT Fm.-Piyuancun&Lantian formation; DY&DST Fm.-Dengying&Doushantuo formation; HCC Fm.- Hongchicun formation; Ages of the first column are from Rooney *et al.* (2015) and references therein, while ages of the column of Central Jiangxi are from this study. a-Condon *et al.*, 2005; b-Zhou *et al.*, 2019; c-Lan *et al.*, 2015a; e-Zhou *et al.*, 2004; c-Ma *et al.*, 1984; d-Lan *et al.*, 2015b; e-Zhou *et al.*, 2004; f-Gao *et al.*, 2013; g-Wang *et al.*, 2012; h-Gao et a., 2014; i-Zhang *et al.*, 2008; j-Zhang *et al.*, 2008; k-Lan *et al.*, 2014; Chen *et al.*, 2009; m-Zhou *et al.*, 2007; m-Lan *et al.*, 2015a; o-Li *et al.*, 2003.

The lower sedimentary sequence below the unconformity is named as the Sibao Group in northern Guangxi province, the Lengjiaxi Group in Hunan province, the Fanjingshan Group in Guizhou province, the Shuangxiwu Group in Zhejiang province, and the Shuangqiaoshan Group in Jiangxi province (Wang and Li., 2003), representing the collision between the Yangtze Block and the Cathaysia Block (Wang *et al.*, 2014). The upper sedimentary sequence above the unconformity consists of sedimentary rocks produced by the Nanhua rifting system that developed at the suture zone between the Yangtze Block and the Cathaysia Block (Fig.S-1).

The Nanhua rifting Basin, from bottom to top, consists of the lower pre-Cryogenian siliciclastic units, the middle Cryogenian glacial and non-glacial deposits and the upper Ediacaran carbonate–siliciclastic rocks (Jiang *et al.*, 2003). The Cryogenian strata in Nanhua rifting basin can be divided into the lower glacial diamictite (the Chang'an/Jiangkou formations and their correlative equivalents), the middle non-glacial shale and siltstone units (the Datangpo Formation and its equivalents), and the upper glacial diamictite (the Nantuo Formation) (Jiang *et al.*, 2003; Zhou *et al.*, 2004; Jiang *et al.*, 2011; Bao *et al.*, 2018). The Chang'an/Jiangkou formations and their correlative equivalents are commonly correlated with the Sturtian glaciation, whereas the Nantuo Formation is correlated with the Marinoan glaciation (e.g., Hoffman and Li, 2009). A number of Neoproterozoic iron formations (IFs) develop in the Nanhua rifting basin (e.g., Fulu and Xinyu IF) (Fig. 1a,c) (Tang, 1987). The Fulu IF was deposited in the shallow-water conditions, whereas the Xinyu BIF was deposited in deep-water settings (Fig. 1a,b) according to its sentimentology characters (Wang and Li, 2003).

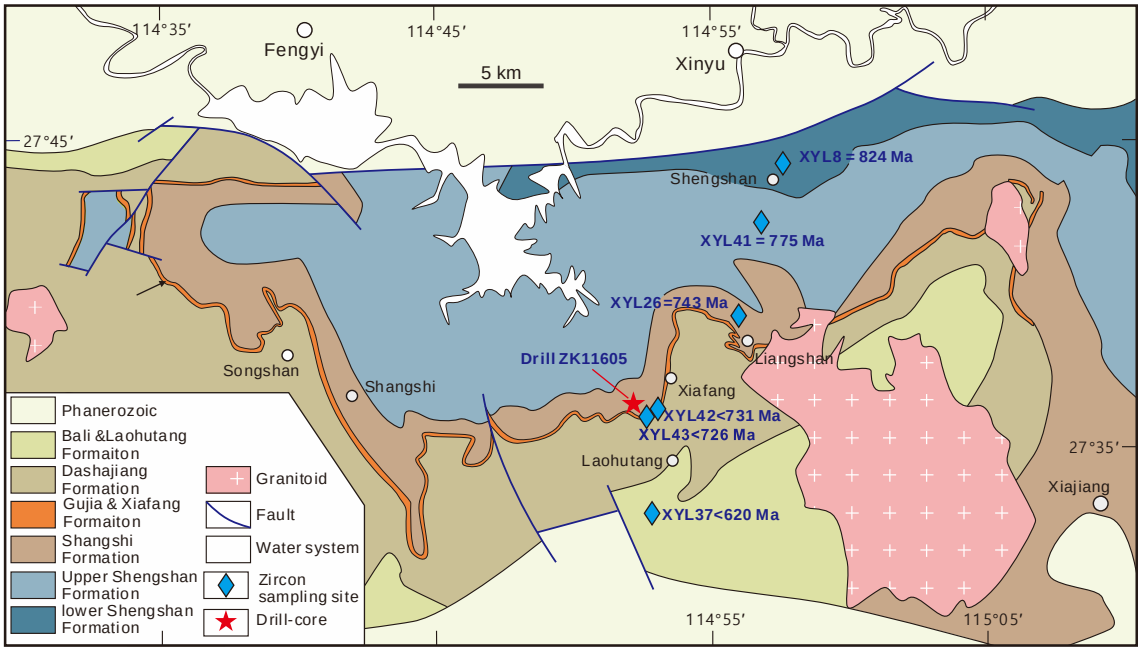

Figure S-2 Geological map of the Xinyu iron formation (Modified from Meng *et al.*, 2017).

Neoproterozoic iron formations from South China exhibit features that are similar to those from eastern Australia and western Laurentia (Eisbacher, 1985; Jiang *et al.*, 2006; Busigny *et al.*, 2018). Major rifting during the late mid-Proterozoic to early Neoproterozoic set the tectonic background for deposition of many of the Neoproterozoic IFs (Fig. 1). The Xinyu Iron Formation was deposited in the central zone of the Nanhua Rift Basin (Fig. 1), underlain by Gujia Formation with pebble-bearing sandy slate and diamictite, with the overlying Dashajiang Formation and Bali Formation (Fig.S-1, Tang *et al.* 1987; Yang *et al.*, 2012).

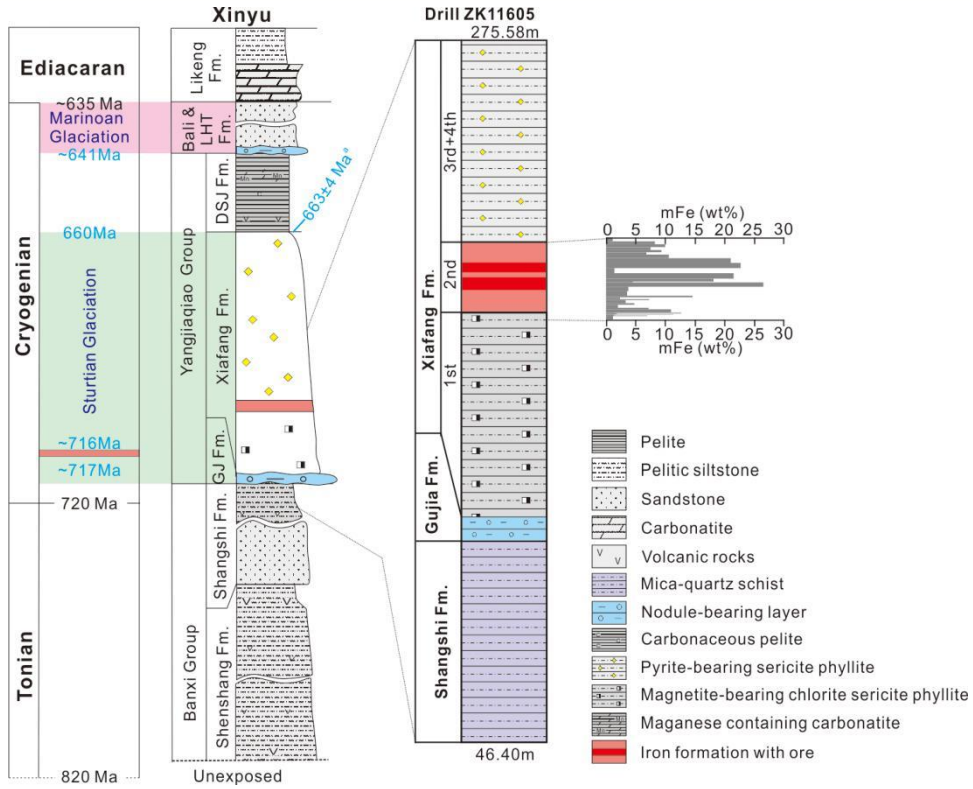

Figure S-3 Variation in lithology and iron content of Xinyu CIF along the drill core ZK11605.

The Sinian system, which contains the Xinyu IF (Fig. S-2), is made up of four unconformity-bounded sequences, that is, the Shengshan formation, the Shangshi formation, the Gujia formation, the Xiafang formation, the Dashajiang formation, the Bali formation, the Laohutang formation and the Likeng formation (Tang *et al.*, 1987, Fig. S-3). The Shengshan formation is mainly sericite phyllite interbedded by several layers of volcanic rocks, while the Shangshi formation is mainly quartz mica schist with some phyllitic sandstone. Both the shengshan and Shangshi formation composed the Banxi group in Central Jiangxi and West Hunan, which is equivalent to the Danzhou Group in North Guanxi and the Xiajiang Group in South Guizhou (Fig. S-1, Song *et al.*, 2017 and references therein). The Yangjiaqiao Group is composed by the lower conglomeratic formation (Gujia Foramtion), the middle ironstone–bearing Xiafang Formation, and the upper manganese-containing Dashajiang Formation (Fig. S3, Yao *et al.*, 1993). The Gujia Formation from the Xinyu area is only several meters thick, and contains magnetite-bearing chlorite sericite phyllite and carbonaceous pseudo-conglomerate. Tang (1987) interpreted the Gujia Formation as an interglacial to glacial deposits Sturtian in age, which is equivalent to the Chang'an formation in North Guangxi and the lower Jiangkou formation in West Hunan (Fig. S-1), correlative with the widespread late Precambrian diamictite strata in South China (Fig. 1c). Contained the Xinyu iron formation, the Xiafang formation is mainly phyllite, which is correlative with the Fulu formation in North Guanxi and the upper Jiangkou formation in West Hunan (Fig. S-1). The Dashajiang Formation contains gravel-containing sericite phyllite with carbon-bearing sericite phyllite, chlorite phyllite, meta-sandstone and manganese carbonate, correlative with the widespread manganese strata of the Datangpo formation in North Guangxi, the Xiangmeng formation in West Hunan (Fig. S-1), which is identified as the interglacial interval between the Sturtian and the Marinoan glaciation (Fig. S-1, Tang *et al.* 1987; Yang *et al.*, 2012).

2. Petrographic and mineralogical features of the Xinyu IF

The Shangshi formation consists of chlorite-sericite phyllite. Widely disseminated magnetite and carbonate occur together with quartz lens that are conformable with oriented muscovite (Fig. S-4a). The Gujia Formation contains magnetite-bearing chlorite sericite phyllite and carbonaceous pseudo-conglomerate (Fig. S-4b). Most carbonaceous pseudo-conglomerate in the formation are ellipsoidal or subrounded in shape, and distribute conformably with their host-sequence (Fig. S-4b).

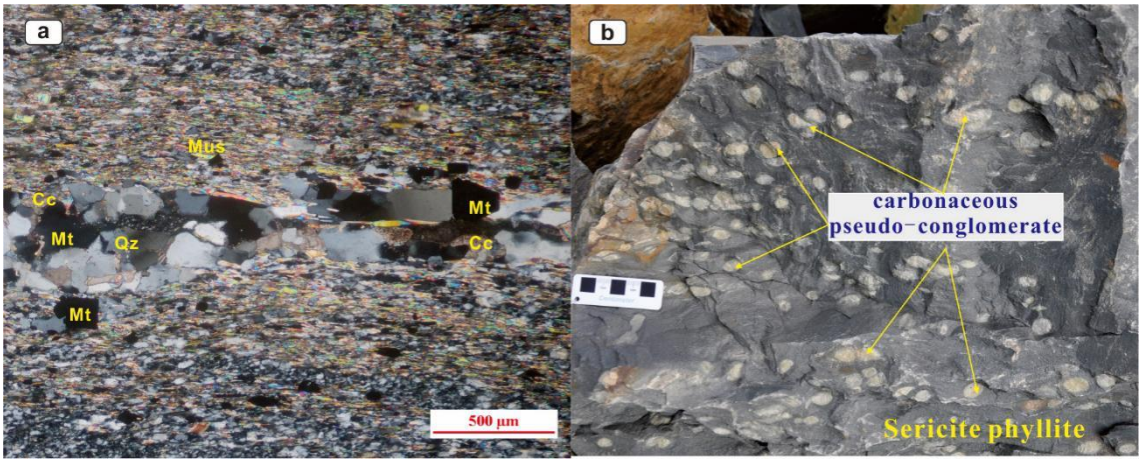

Figure S-4 (a) Microphotograph of the chlorite-sericite phyllite of Shangshi Formation from drill core ZK11605 (cross polarization). **(b)** Photo of Carbonaceous pseudo-conglomerate in magnetite-bearing chlorite sericite phyllite of Gujia Formation. Qz-quartz; Mt- magnetite; Cc-carbonate; Py-pyrite; Ms-muscovite

The Xiafang Formation is composed of three members, which are, stratigraphically upsection, the 1st member that contains magnetite-bearing chlorite sericite phyllite, the 2nd member that is the Xinyu iron formation, and the 3rd member that contains pyrite -bearing chlorite sericite phyllite. The petrographic features of the 1st member are similar to those of the Shangshi formation, that disseminated magnetite grains occur in both quartz veins and the sericite-chlorite matrix, together with interstitial carbonate. The 3rd member is also a chlorite sericite phyllite that share petrographic similarities with the 1st member, except that the iron-bearing mineral is pyrite, instead of magnetite.

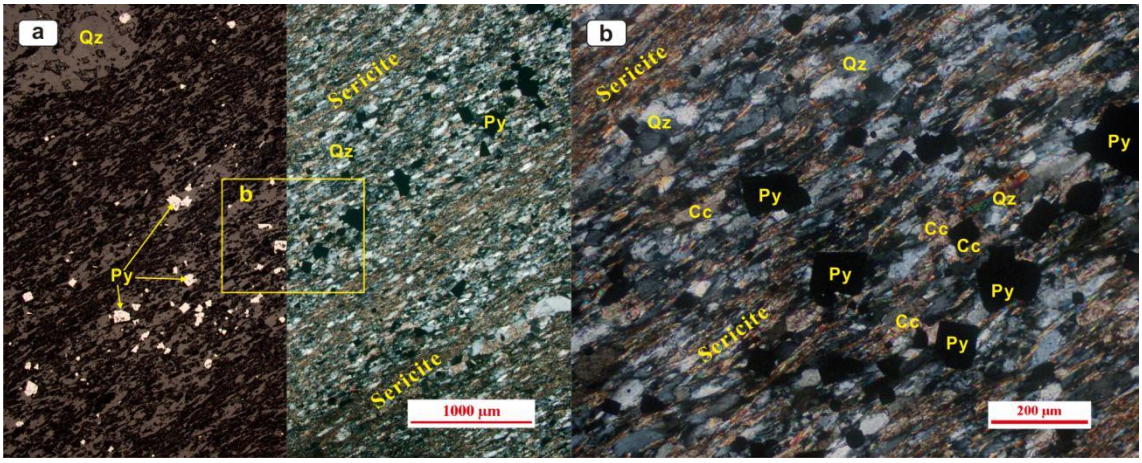

Figure S-5 Microphotographs of the pyrite-bearing sericite phyllite of Xiafang Formation (Left image in plane reflected light).

Quartz and magnetite are the two major constituents for the 2nd member of the Xiafang Formation, the Xinyu iron formation, accounting for more than 90% in volume (Fig. S-6a). The contents of magnetite vary from ca. 5% up to ca. 40% in volume. Beside quartz and magnetite, calcite is also an abundant mineral in the iron formation, while muscovite and chlorite could be found under microscope (Fig. S-6b).

In addition to magnetite, hematite occurs as a minor Fe-oxide phase in some iron formation samples. The hematite grains are generally platy in shape, and display preferred orientation that is conformable with sedimentary beddings, indicating the early diagenetic origin of the hematite. Replacement of hematite by magnetite can be identified in some cases, implying that at least some magnetite grains were produced later than the hematite grains. (Fig. S-6c, d).

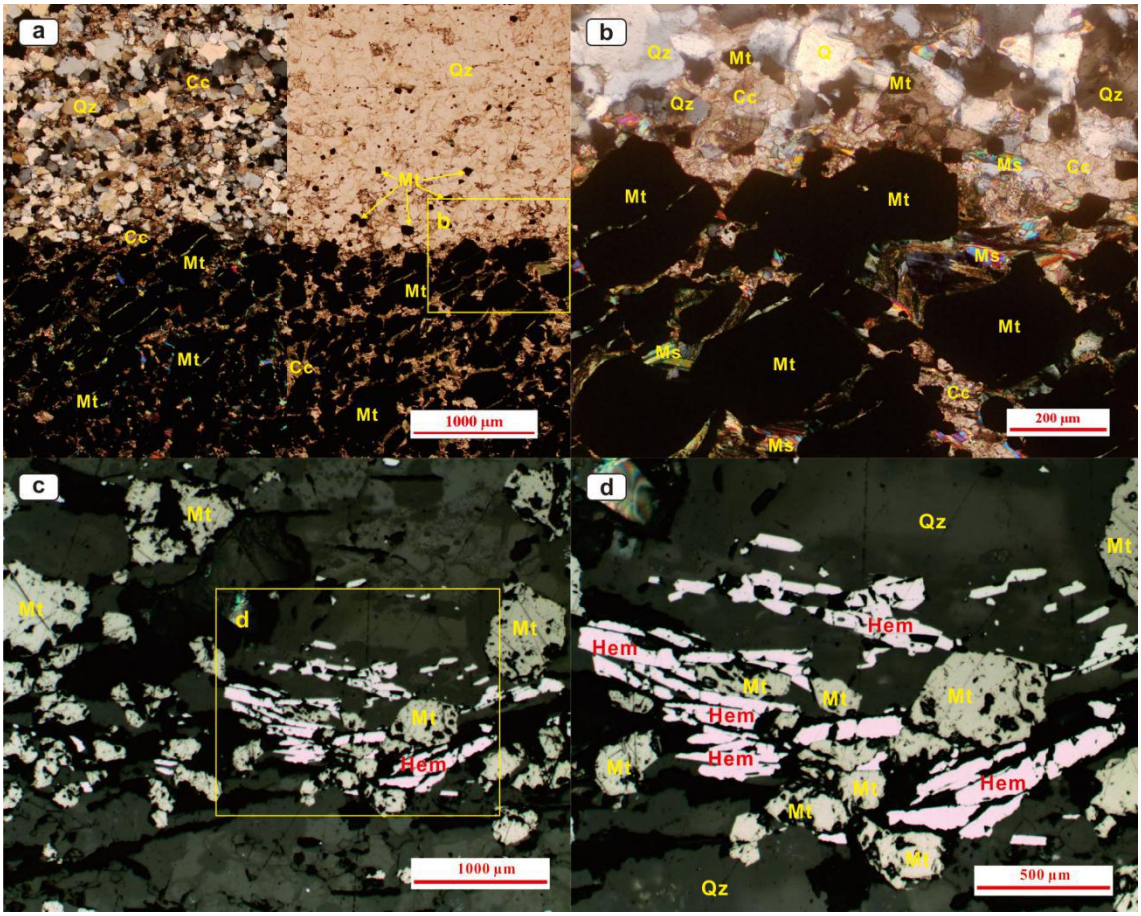

Figure S-6 Photo micrographs of the ironstone from the second member of Xiafang Formation, showing quartz and magnetite-rich bands in **a**, showing characters of quartz, magnetite, carbonates and muscovite in **b**. a-Quartz and magnetite-rich bands in iron formation.b-Zone-in of square in Fig. S-6a, showing characters of quartz, magnetite, calcite and muscovite. **c**-Platy hematite and granular magnetite grains display orientation with sedimentary beddings. **d**-Granular magnetite grain replaces hematite in iron formation band.

Intergrowth of magnetite and carbonates is a common feature in Xinyu iron formation (Fig. S-7). The majority of the interstitial carbonates are ankerite , and a minor proportion of the carbonates are calcite (Fig. S-8).

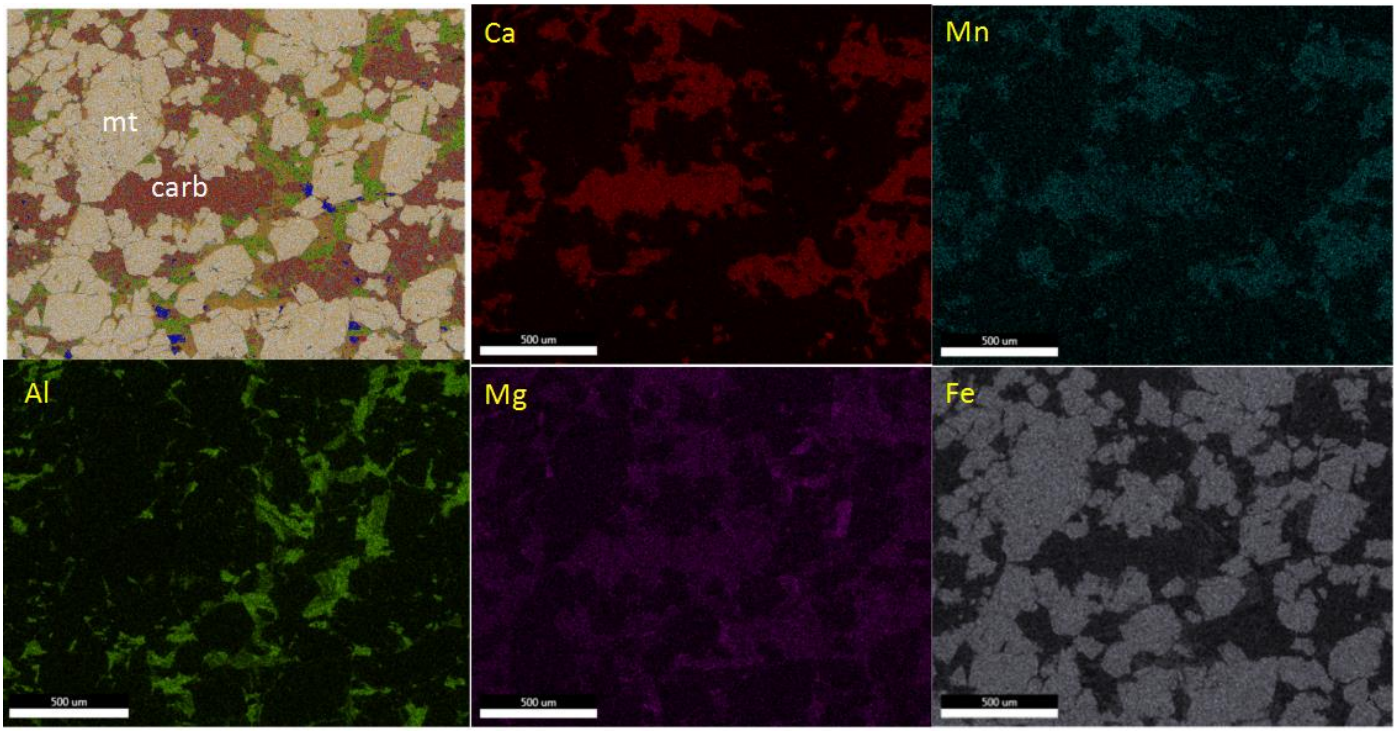

Figure S-7 Elemental mapping (EDS-SEM) of a representative IF sample, which shows intergrowth of magnetite with siderite that contains Ca, Mn, Mg, and Fe.

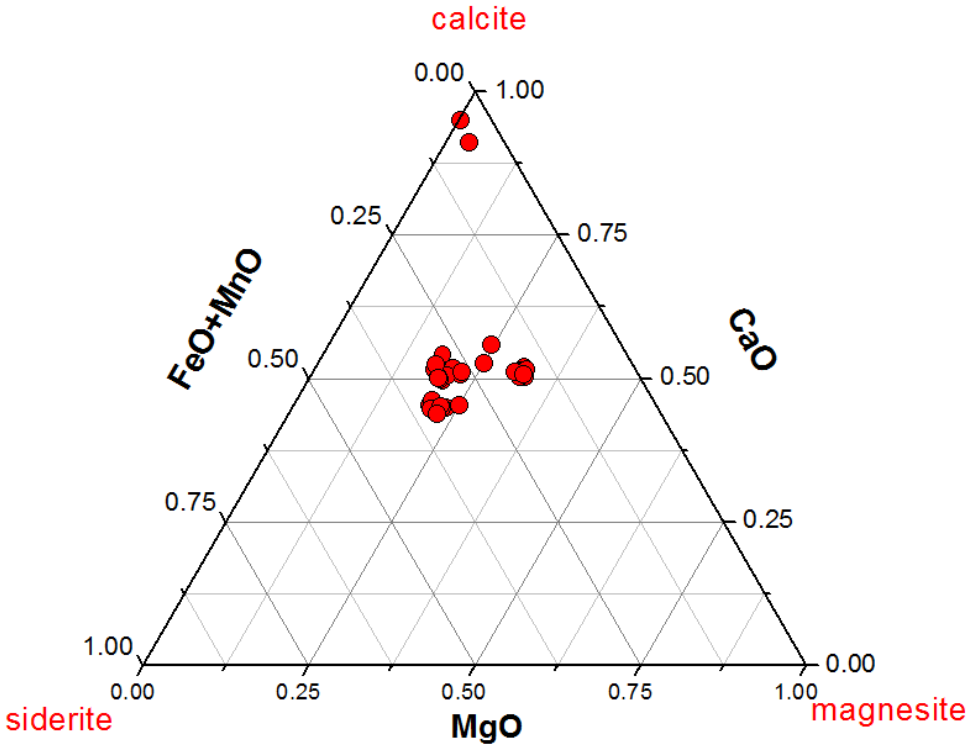

Figure S-8 Tertiary plot of the mineral chemistry of carbonates in samples from drill core ZK11605.

2.1. Evidence of diagenetic origin for the magnetite grains from the Xinyu IF

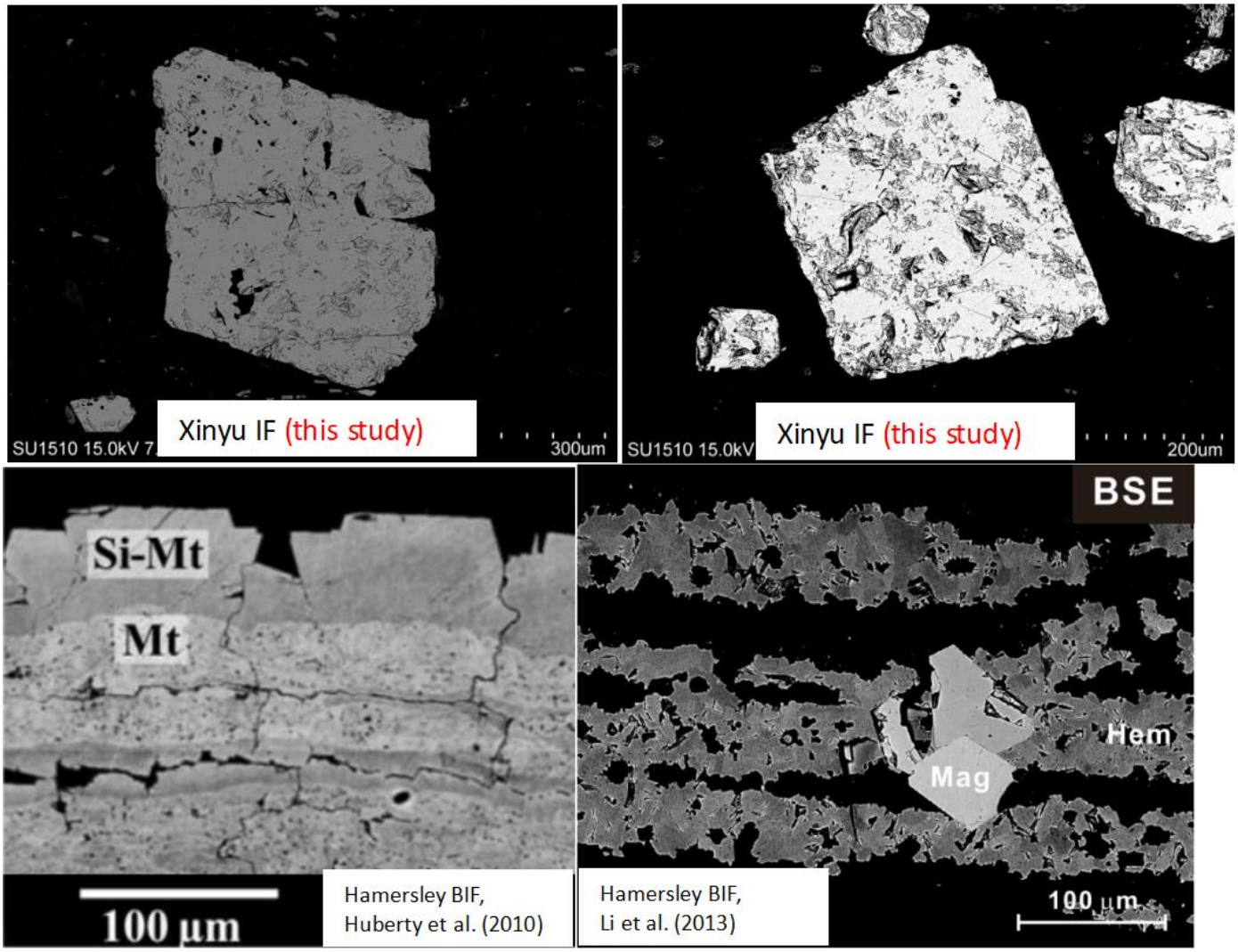

Figure S-9 Comparison of magnetite from Xinyu iron formation (upper two figures), with magnetite from Hamersley banded iron formation in literature (lower two figures). All images were taken using SEM under backscattering model with the highest possible contrast to resolve possible zoning in magnetite.

The magnetite grains from Xinyu IF typically contain numerous microscopic mineral inclusions, and in many cases the apparent large and euhedral magnetite crystals are product of attachment of small crystals. They do not show morphological characteristics of magnetite of metamorphic/hydrothermal origin, which typically lacks mineral inclusions, and show true euhedral crystal habits.

Huberty *et al.* (Huberty *et al.*, 2012) and (Li *et al.*, 2013) showed that metamorphic magnetite in band iron formations are typically silician magnetite, and can form characteristic core-ring textures under backscatter imaging mode under scanning microscope. Fe and O isotope data indicate that the low-Si magnetite cores are of diagenetic origin. Such diagenetic magnetite contains abundant mineral inclusions (see left figure above). By contrast, the silician magnetite form rings on the low-Si magnetite cores or individual crystals are euhedral in shape and clear, lacking mineral inclusions. The core-ring texture is lacking in magnetite grains from the Xinyu IF, indicating that the magnetite in Xinyu IF is not metamorphic in origin.

2.2. Evidence of diagenetic origin for interstitial ankerite from the Xinyu IF

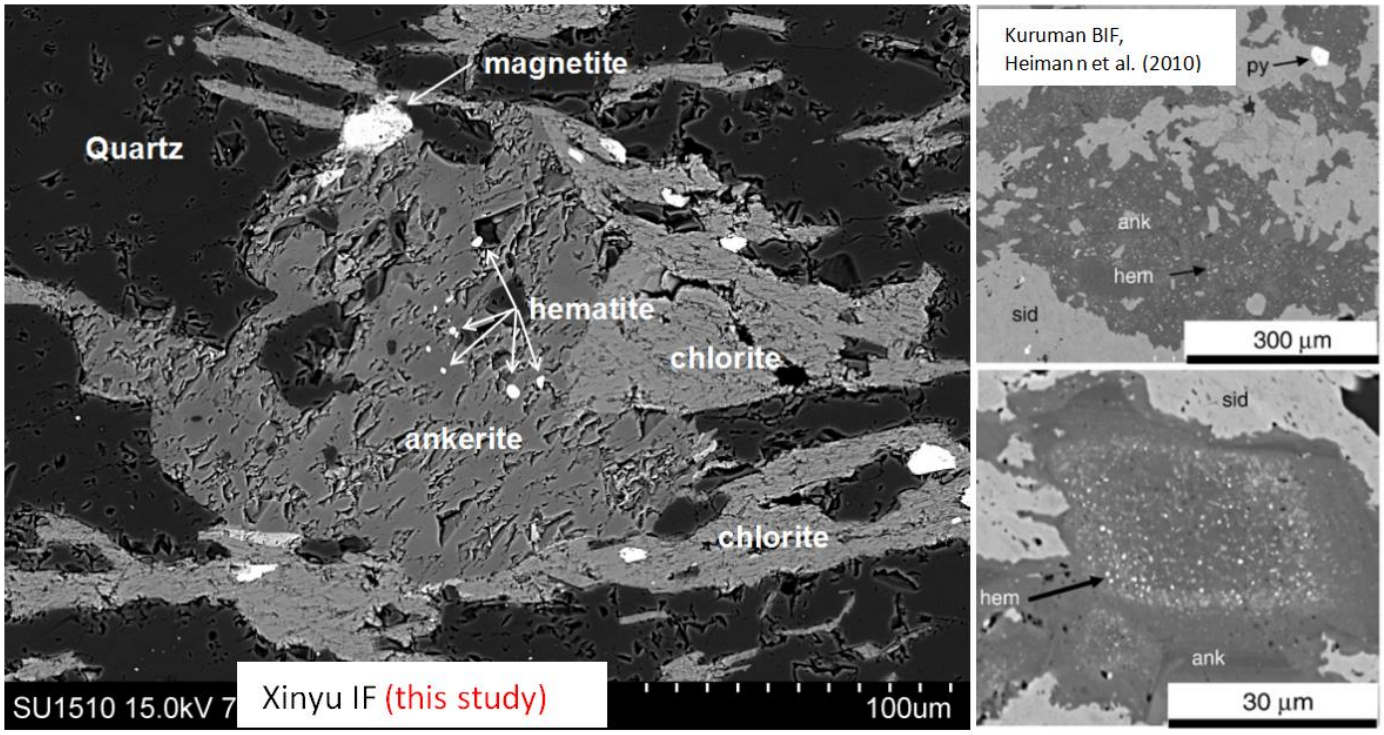

Figure S-10 Comparison of ankerite from Xinyu iron formation (left figures), with ankerite from the Hamersley banded iron formation (two smaller figures in right).

Interstitial carbonates are common in the sedimentary sequence of Xinyu. In the ironstones, interstitial carbonates are mostly ankerite. The ankerite commonly contains disseminated, micro-size hematite inclusions. Such texture has been reported by (Heimann *et al.*, 2010) from the 2.5 Ga Kuruman banded iron formation where ankerite is rigorously proven as early diagenetic via an dissimilatory iron reduction pathway by combined Fe and C isotopes. The hematite mineral inclusions within ankerite are interpreted as remnant of Fe-oxyhydroxide precipitates in soft sediment that was not transformed to ankerite in incomplete dissimilatory iron reduction. Such texture cannot be produced by hydrothermal activity, and has not been reported in literature on hydrothermal ankerite.

3. Analytical Methods and Data Tables

3.1 Iron isotope analysis

Based on petrographic observation, pyrite and magnetite grains were sampled from the drill core chips using a hand-hold microdrill with a tungsten carbide drill bit. Approximately 10mg of the mineral powder for each sample was dissolved and Fe was separated from matrix elements by anion exchange chromatography that followed an established protocol (Du *et al.*, 2017). Recovery of Fe was monitored for every sample by ICP-OES and was always >95% and the total procedural blank of the chemistry was negligible relative to the mass of Fe processed.

Iron isotope ratios were measured using a Thermo Fisher Scientific Neptune Plus MC-ICP-MS at State Key Laboratory for Mineral Deposit Research, Nanjing University. Details about the mass spectrometry has been documented in (Du *et al.*, 2017). Iron isotope compositions are reported as $\delta^{56}Fe$ relative to the international standard of IRMM-014: $\delta^{56}Fe_{sample} = [(^{56}Fe / ^{54}Fe)_{sample} / (^{56}Fe / ^{54}Fe)_{IRMM-014} - 1] \times 1000$ [‰]. The typical internal precision (2standard error or 2SE) was better than ±0.03‰ for $^{56}Fe/^{54}Fe$ and ±0.05‰ for $^{57}Fe/^{54}Fe$. The long-term external reproducibility (2 standard deviation or 2SD) of Fe isotope analysis is better than ±0.06‰ in $^{56}Fe/^{54}Fe$ and ±0.16‰ in $^{57}Fe/^{54}Fe$, based on repeat analysis of multiple Fe isotope standard solutions against in-house stock solutions. Accuracy of Fe isotope measurements was confirmed by repeated measurements of reference samples and USGS rock standards that were treated as unknowns with the IF samples. $\delta^{56}Fe$ of these standards are all consistent with the recommended values in literature within analytical uncertainty (Table S-1).

3.2 Carbon isotope analysis

Approximately 2-10 mg of rock powder was scrapped off the drill core chips from areas where pyrite and magnetite grains were drilled, and was placed in a cleaned and dried quartz tube that was tightly capped with a rubber stopper, and was purged with N_2 before injection of ~ 3 ml of concentrated H_3PO_4 ("104 %"). The tube was thermally equilibrated on an automated heating bench at 70 °C, then reacted for > 36 hours. Carbon isotope compositions were determined using a Finnigan Delta Plus XP continuous flow isotope ratio mass spectrometer in the stable isotope laboratory at Nanjing University. Carbon isotope data are reported using standard δ notation as $\delta^{13}C$ values, using the PDB scales, respectively. All isotope ratios were normalized to the V-PDB standard and reported in per mil (‰). Internal analytical error (2 standard error or 2SE) is less than 0.03‰ for $\delta^{13}C$. External reproducibility was checked by repeat analysis of different in-house carbonate standards and was better than ±0.5‰ for $\delta^{13}C$.

3.3 Sulfur isotope analysis

Based on petrographic observation, pyrite-bearing rocks were sliced and later polished by the polishing papers to get smooth surfaces for in situ sulfur isotope analysis. Sulfur isotope ratios of the pyrite were measured using a Thermo Fisher Scientific Neptune Plus MC-ICP-MS connected to an Electro Scientific Industries NWR193 193 nm ArF excimer laser-ablation system at State Key Laboratory for Mineral Deposit Research, Nanjing University. During the measurement, the pyrite was ablated by the NWR193 excimer laser in the single spot ablation mode with the spot size of 25 μm, the repetition rate of 8 Hz and the energy fluence of 7 J/cm^2. The ablated particles were then transported to MC-ICP-MS for isotope analysis with He as the carrier gas. The MC-ICP-MS was running with medium mass resolution setting to resolve polyatomic interferences of $^{16}O^{16}O^+$ and $^{16}O^{18}O^+$ on $^{32}S^+$ and $^{34}S^+$, respectively. The standard-sample-standard bracketing method was used to correct for the instrumental mass bias and the standard used was pyrite WS-1 whose $\delta^{34}S_{V\text{-}CDT}$ value is 0.3±0.1‰ (Zhu *et al.*, 2017). Each sulfur isotope ratio measurement took about 70s (140 integrations with an integration time of 0.524s), comprising a 20s measurement of baseline (which would be removed by on-peak subtraction), 30s analysis of the standard or samples, and the last 20s for aerosol washout. The typical internal precision (2SE) was better than 0.20‰ for $^{34}S/^{32}S$. Sulfur isotope compositions are reported as $\delta^{34}S$ values relative to Vienna - Cañon Diablo Troilite (V-CDT). The accuracy of the method was assessed by analyses of well-characterized sulfide standards (Balmat sphalerite, $\delta^{34}S$=15.42±0.14‰, 2SD, Kozdon *et al.*, 2010; AgS standard, $\delta^{34}S$=0.07±0.26‰, 2SD, Ding *et al.*, 2001). Despite the difference in matrix, the measured $\delta^{34}S$ values are consistent with the certified values of the respective samples within ±0.5‰ (i.e., Balmat sphalerite, $\delta^{34}S$=15.77±0.36‰, 2SD, n=6, this study; AgS standard, $\delta^{34}S$=-0.51±0.46‰, 2SD, n=5, this study). 0.5‰ is also the 2SD error in $\delta^{34}S$ for repeated analysis on the same sulfide. Therefore, the external analytical uncertainty of our method for $\delta^{34}S$ is estimated to be better than ±0.5‰, such uncertainty is sufficiently small to resolve the >40‰ variability in the Xinyu samples.

Table S-1 Comparison of Fe isotope compositions for USGS rock standards measured in this study with literature values.

Sample	δ^{56}Fe	2SD	δ57Fe	2SD	N
Fe isotope compositions of USGS rock standards measured in this study					
DTS-2b	0.06	0.08	0.08	0.14	3
BHVO-2	0.13	0.05	0.21	0.13	9
BCR-2	0.11	0.08	0.18	0.12	9
Fe isotope compositions of USGS rock standards in literature					
DTS-2b (Craddock and Dauphas, 2011)	0.028	0.042	0.045	0.047	6
BHVO-2 (Craddock and Dauphas, 2011)	0.114	0.035	0.174	0.046	12
BHVO-2 (He *et al.*, 2015)	0.112	0.021	0.163	0.040	27
BHVO-2 (Liu *et al.*, 2014)	0.121	0.049	0.175	0.064	12
BCR-2 (Craddock and Dauphas, 2011)	0.091	0.032	0.126	0.066	8
BCR-2 (He *et al.*, 2015)	0.080	0.024	0.123	0.036	10
BCR-2 (Liu *et al.*, 2014)	0.107	0.025	0.170	0.013	3

Table S-2 Composition of the selected interstitial carbonates in Xinyu IF samples as measured by electron microprobe.

Analysis No.	MnO (wt.%)	MgO (wt.%)	ZnO (wt.%)	SrO (wt.%)	CaO (wt.%)	FeO (wt.%)	Total (wt.%)
1	0.54	10.10	0.05	0.25	29.55	15.42	55.91
2	1.56	12.83	-	0.11	29.55	10.50	54.55
3	1.56	12.71	0.02	0.13	28.97	10.89	54.27
4	0.54	9.99	0.10	0.28	31.59	13.65	56.14
5	1.64	12.88	-	0.12	29.48	11.52	55.64
6	1.39	12.77	-	0.05	29.27	11.26	54.75
7	1.42	12.79	0.01	0.20	28.87	11.19	54.47
8	1.56	13.25	-	0.08	29.67	10.55	55.12
9	1.46	13.37	-	0.09	28.81	11.20	54.92
10	1.44	13.05	0.10	0.17	28.83	11.91	55.49
11	1.31	12.31	-	0.24	28.80	12.00	54.65
12	1.32	13.02	0.05	0.11	28.87	11.32	54.69
13	2.22	1.52	0.03	0.29	52.51	1.63	58.19

14	3.05	0.15	0.06	0.09	55.82	0.37	59.54
15	2.97	8.81	0.11	0.19	27.64	15.69	55.40
16	3.95	8.16	0.03	0.30	28.30	15.13	55.86
17	1.28	7.38	0.02	0.12	30.62	18.94	58.36
18	3.10	8.01	0.14	0.19	27.09	17.98	56.50
19	3.33	8.01	0.03	0.18	27.49	16.86	55.90
20	3.54	7.52	-	0.18	27.20	17.54	55.98
21	3.10	7.68	0.04	0.18	26.75	17.80	55.54
22	1.47	6.95	-	0.23	28.40	19.08	56.13
23	3.81	7.57	0.06	0.09	27.09	17.30	55.92
24	2.75	8.76	0.03	0.22	27.76	15.65	55.17
25	17.05	9.52	0.01	0.09	26.49	7.68	60.81
26	16.39	8.59	0.05	0.12	26.52	8.98	60.63
27	15.25	8.98	-	0.11	24.19	6.59	55.12
28	15.79	8.26	-	0.07	26.05	8.14	58.30
29	15.94	9.07	0.01	0.16	24.98	7.09	57.24
30	17.82	9.03	-	0.19	26.65	8.26	61.94
31	17.05	9.75	0.06	0.08	27.53	8.12	62.58
32	16.82	8.91	0.02	0.13	24.25	6.89	57.00

Table S-3 Iron, sulfur and carbon isotope composition for Iron formations of the Xinyu IF.

Samples	Depth (m)	$\delta^{56}Fe$ (‰)	2SD	$\delta^{57}Fe$ (‰)	2SD	N	$\delta^{13}C$ (‰, PDB)	2SD	N	$\delta^{34}S$ (‰, CDT)	2SE
Chlorite muscovite schist of the upper Shangshi formation											
ZK11605-02	59.6	0.12	0.03	0.2	0.05	1					
ZK11605-03	94.0	0.09	0.02	0.17	0.04	1					
Carbonaceous pseudo-conglomerate-contained chlorite sericite phyllite of Gujia Formation											
ZK11605-04	114.6	0.11	0.02	0.28	0.05	1	-6.54	0.03	3		
ZK11605-05	114.7	0.15	0.02	0.24	0.04	1	-6.48	0.13	1		
ZK11605-06	114.8						-6.81	0.07	1		
ZK11605-07	117.0	0.19	0.02	0.25	0.04	1					
Magnetite-bearing chlorite sericite phyllite of the fist member of Xiafang Formation											
ZK11605-08	120.7	0.06	0.02	0.13	0.04	1	-7.17	0.05	2		
ZK11605-09	125.6	0.22	0.02	0.39	0.04	1	-8.00	0.11	3		
ZK11605-10	136.9	0.39	0.02	0.69	0.05	1	-6.96	0.10	1		
ZK11605-11	160.4	0.14	0.02	0.19	0.04	1	-8.26	0.07	2		
ZK11605-12	166.0	-0.09	0.02	-0.14	0.05	1	-8.00	0.02	2		
ZK11605-13	174.8	-0.04	0.02	-0.08	0.05	1	-7.90	0.09	1		
ZK11605-14	177.5	-0.06	0.02	-0.06	0.04	1	-7.85	0.09	2		
ZK11605-15	184.5	0.21	0.03	0.40	0.05	1	-8.24	0.11	2		
ZK11605-16	184.8	0.27	0.03	0.40	0.05	1					
ZK11605-17	189.0	0.41	0.14	0.59	0.12	2	-8.41	0.06	1		
ZK11605-18	190.0	-0.02	0.01	-0.04	0.06	2	-8.69	0.12	1		
ZK11605-19	192.2						-6.71	0.03	1		
ZK11605-20	194.2	0.52	0.07	0.8	0.01	2	-8.29	0.05	1		
ZK11605-21	196.4	0.39	0.01	0.62	0.01	2					
ZK11605-22	197.0	0.95	0.02	1.41	0.02	2	-8.47	0.01	3		
Iron formation of the second member of Xiafang Formation											
ZK11605-23	197.9	0.08	0.04	0.10	0.00	2					
ZK11605-24	199.1	0.14	0.00	0.27	0.03	2					
ZK11605-25	201.1	0.35	0.02	0.49	0.14	2					

ZK11605-26	202.1	0.63	0.01	0.95	0.13	2					
ZK11605-27	202.9	0.16	0.05	0.26	0.22	2	-9.46	0.07	1		
ZK11605-28	204.4	0.78	0.01	1.16	0.07	2	-9.36	0.11	3		
ZK11605-29	205.5	1.53	0.04	2.26	0.07	2	-9.73	0.06	2		
ZK11605-30	206.5	1.67	0.01	2.49	0.02	2	-9.62	0.03	3		
ZK11605-32	208.7	1.61	0.06	2.4	0.03	2	-9.46	0.1	1		
ZK11605-33	209.7	1.55	0.00	2.35	0.03	2	-10.48	0.03	1		
ZK11605-34	210.7	2.10	0.20	3.17	0.02	2	-11.68	0.23	1		
ZK11605-36	214.7	1.01	0.02	1.41	0.02	2					
Pyrite-bearing sericite phyllite of the third and fourth members of Xiafang Formation											
ZK11605-37	218.0	0.29	0.06	0.46	0.19	2	-7.07	0.02	2	-41.81	0.14
ZK11605-38	220.0	0.84	0.03	1.27	0.05	2	-7.19	0.08	2	-29.1	0.10
										-29.8	0.11
										-29.57	0.13
										-29.47	0.10
ZK11605-39	222.0	0.73	0.07	1.12	0.27	2	-9.09	0.08	2	-25.32	0.13
										-25.96	0.16
ZK11605-40	225.0	0.59	0.01	0.93	0.03	2	-8.08	0.09	1	-17.14	0.13
										-16.58	0.09
										-15.26	0.11
										-17.2	0.11
ZK11605-41	227.0	0.46	0.03	0.68	0.07	2	-7.42	0.18	1	-16.28	0.13
										-15.71	0.10
										-16.18	0.10
										-16.35	0.12
ZK11605-42	230.0	0.23	0.00	0.36	0.03	2	-7.60	0.02	3	-15.49	0.11
										-15.46	0.12
										-12.55	0.13
ZK11605-43	232.0	0.38	0.06	0.64	0.01	2	-7.64	0.07	1		
ZK11605-44	236.5	0.50	0.03	0.78	0.12	2	-7.40	0.01	2	-10.37	0.15
										-9.85	0.13
ZK11605-45	239.0									-4.33	0.23

ZK11605-46	240.0	0.37	0.00	0.50	0.22	2	-7.71	0.07	1	-4.24	0.16
										-3.92	0.13
ZK11605-47	243.0	0.24	0.00	0.41	0.1	2	-7.89	0.06	2	-14.98	0.13
										-14.83	0.19
ZK11605-48	245.5	0.29	0.03	0.45	0.05	2	-7.91	0.05	3	-10.38	0.12
										-12.01	0.15
ZK11605-49	246.0									-8.28	0.12
										-10.66	0.12
										-9.90	0.13
										-10.64	0.13
ZK11605-50	249.0	0.07	0.01	0.09	0.15	2	-6.42	0.07	1	-1.89	0.11
										-5.33	0.10
										-5.39	0.10
										-2.27	0.10
ZK11605-51	252.0	0.30	0.03	0.46	0.07	2	-8.03	0.05	1	1.17	0.13
										1.26	0.13
										0.81	0.13
										1.44	0.13
ZK11605-52	254.0	0.80	0.08	1.25	0	2	-7.9	0.08	1	3.21	0.14
										3.83	0.13
										3.47	0.14
										3.16	0.12
ZK11605-53	257.0									3.01	0.15
										2.16	0.12
										2.42	0.10
										2.88	0.10
ZK11605-54	260.0									3.10	0.12
										2.86	0.12
										2.94	0.12
										2.88	0.13
ZK11605-55	263.0									4.19	0.10
										4.48	0.11

										4.72	0.11
										4.34	0.19
ZK11605-56	266.5									5.07	0.12
										5.16	0.11
										3.91	0.11
										4.35	0.13
ZK11605-57	268.0									1.76	0.12
										1.92	0.13
										1.76	0.12
										1.59	0.13
ZK11605-58	270.0	0.42	0.02	0.61	0.11	2	-7.85	0.1	1	0.97	0.13
										0.97	0.18
										0.76	0.13
										1.07	0.15
ZK11605-59	272.0	0.34	0.07	0.57	0.11	2	-7.99	0.07	2	-0.68	0.12
										-0.89	0.13
										-0.94	0.13
										-1.00	0.11

Supplementary Information References

Bao, X., Zhang, S., Jiang, G., Wu, H., Li, H., Wang, X., An, Z. Yang, T. (2018) Cyclostratigraphic constraints on the duration of the Datangpo Formation and the onset age of the Nantuo (Marinoan) glaciation in South China. *Earth and Planetary Science Letters* 483, 52–63.

Busigny, V., Planavsky, N.J., Goldbaum, E., Lechte, M.A., Feng, L., Lyons, T.W. (2018) Origin of the Neoproterozoic Fulu iron formation, South China: Insights from iron isotopes and rare earth element patterns. *Geochimica et Cosmochimica Acta* 242, 123–142.

Chen, D., Wang, J., Qing, H., Yan, D., Li, R. (2009) Hydrothermal venting activities in the Early Cambrian, South China: petrological, geochronological and stable isotopic constraints. *Chemical Geology* 258, 168–181.

Condon, D., Zhu, M., Bowring, S., Wang, W., Yang, A., Jin, Y. (2005) U-Pb ages from the neoproterozoic Doushantuo Formation, China. *Science* 308, 95–98.

Craddock P.R., Dauphas N. (2011) Iron isotopic compositions of geological reference materials and chondrites. *Geostandards And Geoanalytical Research* 35, 101–123.

Ding, T., Vaikiers, S., Wan, D., Bai, R., Zou, X., Li, Y., Zhang, Q., De Bievre, P. (2001) The 33S and 34S values and absolute 32S/33S and 32S/34S ratios of IAEA and Chinese sulfur isotope reference materials (in Chinese with English abstract). Bulletin of Mineralogy, *Petrology and Geochemistry* 20, 425–427.

Du, D.H., Wang, X.L., Yang, T., Chen, X., Li, J.Y., Li, W. (2017) Origin of heavy Fe isotope compositions in high-silica igneous rocks: A rhyolite perspective. *Geochimica et Cosmochimica Acta* 218, 58–72.

Eisbacher, G.H. (1985) Late Proterozoic rifting, glacial sedimentation, and sedimentary cycles in the light of Windermere deposition, western Canada. *Palaeogeography, Palaeoclimatology, Palaeoecology* 51, 231–254.

Gao, L.Z., Chen, J.S., Dai, C.G., Ding, X.Z., Wang, X.H., Liu, Y.X. (2014). SHRIMP zircon U-Pb dating of tuff in Fanjingshan Group and Xiajiang Group from Guizhou and Hunan Provinces and its stratigraphic implications. *Geological Bulletin of China*, 33(7), 949-959.

Gao, L.Z., Lu, J.P., Ding, X.Z., Wang, H.R., Liu, Y.X., Li, J. (2013) Zircon U–Pb dating of Neoproterozoic tuff in South Guangxi and its implications for stratigraphic correlation. *Geology in China* 40(5), 1443–1452.

Gao, W., Zhang, C.H. (2009) Zircon SHRIMP U-Pb ages of the Huangling granite and the tuff beds from Liantuo Formation in the Three Gorges area of Yangtze River, China and its geological significance. *Geological Bulletin of China* 28, 45–50.

Ge, W. C., Li, X.H., Li, Z.X., Zhou, H.W. (2001) Mafic intrusions in Longsheng area: age and its geological implications. *Chinese Journal of Geology* 36, 112–118 (in Chinese with English abstract).

Heimann, A., Johnson, C.M., Beard, B.L., Valley, J.W., Roden, E.E., Spicuzza, M.J., Beukes, N.J. (2010) Fe, C, and O isotope compositions of banded iron formation carbonates demonstrate a major role for dissimilatory iron reduction in ~ 2.5 Ga marine environments. *Earth and Planetary Science Letters* 294, 8–18.

Hoffman, P.F. Li, Z.X., (2009) A palaeogeographic context for Neoproterozoic glaciation. *Palaeogeography Palaeoclimatology Palaeoecology* 277, 158–172.

Hu, Z.Y., Hu, W.X., Wang, X.M., Lu, Y.Z., Wang, L.C., Liao, Z.W., Li, W.Q. (2017) Resetting of Mg isotopes between calcite and dolomite during burial metamorphism: Outlook of Mg isotopes as geothermometer and seawater proxy. *Geochimica et Cosmochimica Acta* 208, 24–40.

Huberty, J.M., Konishi, H., Heck, P.R., Fournelle, J.H., Valley, J.W., Xu, H. (2012) Silician magnetite from the Dales Gorge Member of the Brockman Iron Formation, Hamersley Group, Western Australia. *American Mineralogist* 97, 26–37.

Ilyin, A.V. (2009) Neoproterozoic banded iron formations. *Lithology and Mineral Resources* 44, 78–86.

Jiang, G., Kennedy, M.J., Christie-Blick, N., Wu, H., Zhang, S. (2006) Stratigraphy, sedimentary structures, and textures of the late Neoproterozoic Doushantuo cap carbonate in South China. *Journal of Sedimentary Research* 76, 978–995.

Jiang, G., Shi, X., Zhang, S., Wang, Y., Xiao, S. (2011) Stratigraphy and paleogeography of the Ediacaran Doushantuo Formation (ca. 635-551 Ma) in South China. *Gondwana Research* 19, 831–849.

Jiang, G.Q., Sohl, L.E., Christie-Blick, N. (2003) Neoproterozoic stratigraphic comparison of the Lesser Himalaya (India) and Yangtze block (south China): Paleogeographic implications. *Geology* 31, 917–920.

Kozdon, R., Kita, N.T., Huberty, J.M., Fournelle, J.H., Johnson, C.A., Valley, J.W. (2010) In situ sulfur isotope analysis of sulfide minerals by SIMS: Precision and accuracy, with application to thermometry of ~3.5Ga Pilbara cherts. *Chemical Geology* 275, 243-253.

Lan, Z., Li, X.H., Zhang, Q., Li, Q.L. (2015a) Global synchronous initiation of the 2nd episode of Sturtian glaciation: SIMS zircon U–Pb and O isotope evidence from the Jiangkou Group, South China. *Precambrian Research* 267, 28–38.

Lan, Z., Li, X.H., Zhu, M., Zhang, Q., Li, Q.L. (2015b) Revisiting the Liantuo Formation in Yangtze Block, South China: SIMS U–Pb zircon age constraints and regional and global significance. *Precambrian Research* 263, 123–141.

Lan, Z., Li, X., Zhu, M., Chen, Z.Q., Zhang, Q., Li, Q., Lu, D., Liu, Y., Tang, G. (2014) A rapid and synchronous initiation of the wide spread Cryogenian glaciations. *Precambrian Research* 255, 401–411.

Li, W., Huberty, J.M., Beard, B.L., Kita, N.T., Valley, J.W., Johnson, C.M. (2013) Contrasting behavior of oxygen and iron isotopes in banded iron formations revealed by in situ isotopic analysis. *Earth and Planetary Science Letters* 384, 132–143.

Li, Z.X., Li, X.H., Kinny, P.D., Wang, J., Zhang, S., Zhou, H. (2003) Geochronology of Neoproterozoic syn-rift magmatism in the Yangtze Craton, South China and correlations with other continents: evidence for a mantle superplume that broke up Rodinia. *Precambrian Research* 122, 85–109

Liu S. A., Li D., Li S., Teng F. Z., Ke S., He Y., Lu, Y. (2014) High-precision copper and iron isotope analysis of igneous rock standards by MC-ICP-MS. *Journal of Analytical Atomic Spectrometry* 29, 122–133.

Ma, G., Li, H., Zhang, Z. (1984) An investigation of the age limits of the Sinian System in South China. *Bulletin of Yichang Institute of Geology and Mineral Resources* 8, 1–29.

Macdonald, F.A., Schmitz, M.D., Crowley, J.L., Roots, C.F., Jones, D.S., Maloof, A.C., Strauss, J.V., Cohen, P.A., Johnston, D.T., Schrag, D.P. (2010) Calibrating the cryogenian. *Science* 327(5970), 1241–1243.

Meng, C., Wu, C., Qin, H., Chi, Z., Yang, Z., Lei, R., Lou, F., Xie, G. (2017) In situ major and trace element geochemistry of magnetite: implication for ore formation processes and mechanism of the Liangshan iron deposit, Xinyu, China. *Geological Journal of China Universities* 23, 181–193.

Shu, L.S., Faure, M., Yu, J.H., Jahn, B.M. (2011) Geochronological and geochemical features of the Cathaysia block (South China): New evidence for the Neoproterozoic breakup of Rodinia. *Precambrian Research* 187, 263–276.

Song, G., Wang, X., Shi, X., Jiang, G. (2017) New U-Pb age constraints on the upper Banxi Group and synchrony of the Sturtian glaciation in South China. *Geoscience Frontiers* 8, 1161–1173.

Tang, J., Fu, H., Yu, Z. (1987) Stratigraphy, type and formation conditions of the Late Precambrian banded iron ores in South China. *Chinese Journal of Geochemistry* 6, 331–341.

Wang, J. Li, Z.X. (2003) History of Neoproterozoic rift basins in South China: implications for Rodinia break-up. *Precambrian Research* 122, 141–158.

Wang, W., Zhou, M.F., Yan, D.P., Li, J.W. (2012) Depositional age, provenance, and tectonic setting of the Neoproterozoic Sibao Group, southeastern Yangtze Block, South China. *Precambrian Research* 192-95, 107–124.

Wang, X.C., Li, X.H., Li, Z.X., Li, Q.L., Tang, G.Q., Gao, Y.Y., Zhang Q.R., Liu, Y. (2012) Episodic Precambrian crust growth: evidence from U–Pb ages and Hf–O isotopes of zircon in the Nanhua Basin, central South China. *Precambrian Research* 222, 386–403.

Wang, X.L., Zhou, J.C., Griffin, W.L., Zhao, G., Yu, J.H., Qiu, J.S., Zhang, Y.J. Xing, G.F. (2014) Geochemical zonation across a Neoproterozoic orogenic belt: Isotopic evidence from granitoids and metasedimentary rocks of the Jiangnan orogen, China. *Precambrian Research* 242, 154–171.

Yang, M.G., Liu, Y.G., Huang, Z.Z., Wu, F.J., Song, Z.R. (2012) Subdivision of Meso-Neoproterozoic strata in Jiangxi and a correlation with the neighboring areas. *Geology in China* 39, 43–53.

Yao, P., Wang, K.N., Du, C.L., Lin, Z.T., Song, X. (1993) Records of China's iron ore deposits. Beijing, *Metallurgical Industry Press* pp 660.

He Y., Ke S., Teng F. Z., Wang T., Wu H., Lu Y., Li S. (2015) High-precision iron isotope analysis of geological reference materials by high-resolution MC-ICP-MS. *Geostandards And Geoanalytical Research* 39, 341–356.

Yu, J.H., O'Reilly, S.Y., Wang, L., Griffin, W.L., Zhou, M.-F., Zhang, M., Shu, L. (2010) Components and episodic growth of Precambrian crust in the Cathaysia Block, South China: Evidence from U-Pb ages and Hf isotopes of zircons in Neoproterozoic sediments. *Precambrian Research* 181, 97–114.

Zhang, Q.R., Li, X.H., Feng, L.J., Huang, J., Song, B. (2008) A new age constraint on the onset of the Neoproterozoic glaciations in the Yangtze Platform, South China. *The Journal of Geology* 116, 423–429.

Zhang, S., Jiang, G., Han, Y. (2008) The age of the Nantuo Formation and Nantuo glaciation in South China. *Terra Nova* 20, 289–294.

Zhang, S., Jiang, G., Dong, J., Han, Y., Wu, H. (2008) New SHRIMP U-Pb age from the Wuqiangxi Formation of Banxi Group: Implications for rifting and stratigraphic erosion associated with the early Cryogenian (Sturtian) glaciation in South China. *Science in China Series D: Earth Sciences* 51, 1537–1544.

Zhao, G., Cawood, P.A. (2012) Precambrian geology of China. *Precambrian Research* 222, 13–54.

Zhao, G.C., Wilde, S.A., Cawood, P.A., Sun, M. (2001) Archean blocks and their boundaries in the North China Craton: lithological, geochemical, structural and P-T path constraints and tectonic evolution. *Precambrian Research* 107, 45–73.

Zheng, J.P., Griffin, W.L., O'Reilly, S.Y., Zhang, M., Pearson, N., Pan, Y.M. (2006) Widespread Archean basement beneath the Yangtze craton. *Geology* 34, 417–420.

Zhou, C., Huyskens, M.H., Lang, X., Xiao, S., Yin, Q.Z. (2019) Calibrating the terminations of Cryogenian global glaciations. *Geology* 47, 251–254.

Zhou, C.M., Tucker, R., Xiao, S.H., Peng, Z.X., Yuan, X.L., Chen, Z. (2004) New constraints on the ages of Neoproterozoic glaciations in south China. *Geology* 32, 437–440.

Zhou, J., Li, X. H., Ge, W., Li, Z.X. (2007) Age and origin of middle Neoproterozoic mafic magmatism in southern Yangtze Block and relevance to the break-up of Rodinia. *Gondwana Research* 12, 184–197.

Zhu, Z.-Y., Jiang, S.-., Ciobanu, C.L., Yang, T., Cook, N.J. (2017) Sulfur isotope fractionation in pyrite during laser ablation: Implications for laser ablation multiple collector inductively coupled plasma mass spectrometry mapping. *Chemical Geology* 450, 223-234.